

Practical implementation of dynamic methods for measuring atomic force microscope cantilever spring constants

This article has been downloaded from IOPscience. Please scroll down to see the full text article.

2006 Nanotechnology 17 2135

(<http://iopscience.iop.org/0957-4484/17/9/010>)

[The Table of Contents](#) and [more related content](#) is available

Download details:

IP Address: 132.163.130.71

The article was downloaded on 29/03/2010 at 19:25

Please note that [terms and conditions apply](#).

Practical implementation of dynamic methods for measuring atomic force microscope cantilever spring constants

S M Cook^{1,2}, T E Schäffer³, K M Chynoweth^{1,2}, M Wigton^{1,2},
R W Simmonds² and K M Lang^{1,2}

¹ Department of Physics, Colorado College, Colorado Springs, CO 80903, USA

² National Institute of Standards and Technology, 325 Broadway, Boulder, CO 80305, USA

³ Center for Nanotechnology and Institute of Physics, Westfälische Wilhelms-Universität Münster, Gievenbecker Weg 11, 48149 Münster, Germany

E-mail: tilman.schaeffer@uni-muenster.de and kmlang@coloradocollege.edu

Received 26 October 2005, in final form 16 February 2006

Published 28 March 2006

Online at stacks.iop.org/Nano/17/2135

Abstract

Measurement of atomic force microscope cantilever spring constants (k) is essential for many of the applications of this versatile instrument. Numerous techniques to measure k have been proposed. Among these, we found the thermal noise and Sader methods to be commonly applicable and relatively user-friendly, providing an *in situ*, non-destructive, fast measurement of k for a cantilever independent of its material or coating. Such advantages recommend these methods for widespread use. An impediment thereto is the significant complication involved in the initial implementation of the methods. Some details of the implementation are discussed in publications, while others are left unsaid. Here we present a complete, cohesive, and practically oriented discussion of the implementation of both the thermal noise and Sader methods of measuring cantilever spring constants. We review the relevant theory and discuss practical experimental means for determining the required quantities. We then present results that compare measurements of k by these two methods over nearly two orders of magnitude, and we discuss the likely origins of both statistical and systematic errors for both methods. In conclusion, we find that the two methods agree to within an average of 4% over the wide range of cantilevers measured. Given that the methods derive from distinct physics we find the agreement a compelling argument in favour of the accuracy of both, suggesting them as practical standards for the field.

1. Introduction

Atomic force microscopy (AFM) and its variants are a prevalent method of characterizing not only topographic but also electrical, magnetic, and structural properties of materials. For many such applications, knowledge and control of the forces exerted by the AFM cantilever are essential. For example, in conducting atomic force microscopy (CAFM), it has been demonstrated that the scanning force determines the contact area of the tip on the surface, which in turn gives the local current [1, 2]. In other experiments, measurement

of forces is the end goal, such as in single-molecule force spectroscopy studies of molecular binding forces [3–8] and of intramolecular folding forces [9–11].

The primary impediment to accurate measurement of forces in AFM is measurement of the cantilever spring constants. Numerous methods have been proposed to measure AFM cantilever spring constants, and we briefly mention some here. *Dimensional methods* require precise knowledge of the cantilever dimensions and material [12]. *Static experimental methods* employ deflection by calibrated standards [13–15], glass fibres [16, 17] or added mass [18].

Dynamic experimental methods detect the shift in resonant frequency caused by an added mass [19], utilize thermal vibration noise [20–28], employ knowledge of cantilever mass and resonance frequency [29], or are derived from fluid dynamics theory [30, 31]. A recent review nicely summarizes many of them [32].

After consideration of all methods, we chose two methods, the ‘thermal noise method’ [20–28] and the ‘Sader method’ [30, 31], because they were commonly applicable and relatively easy to use, with reported accuracies comparable to those of other methods [12, 32]. More specifically, the advantages of these methods are: (1) both methods provide an *in situ* measurement of the spring constant; (2) both methods are applicable to cantilevers independent of material or coating; (3) both require minimal hardware and software that is standard in many laboratories or inexpensively purchased; (4) both are nondestructive and noninvasive; (5) once the appropriate hardware and software are in place, both provide quick results and can be used by an operator with minimal training; and finally, (6) the two methods require substantially the same hardware and software, rendering their simultaneous implementation straightforward.

Although both the thermal and Sader methods are easy to use once realized, their initial implementation is complicated. Some details of implementation are discussed in scattered publications, while others are left unsaid or unclear. To address this situation, one goal of this paper is to present a complete and cohesive guide to implementation of the thermal noise and Sader methods of measuring spring constants for rectangular cantilevers. This goal is met by inclusion of the extensively detailed and pedagogic sections 2–4 which include a thorough discussion of both experimental and theoretical factors that need be considered.

Using these two methods we measured a variety of rectangular cantilevers with spring constants spanning almost two orders of magnitude, from 0.1 to 7 N m^{−1}. A second goal of this paper is to compare the results of the two methods over this wide range of conditions. As these two methods are derived from distinct physics—the thermal method from fundamental statistical mechanics and the Sader method from fluid dynamics—agreement of the methods is a strong statement in favour of their validity.

We begin in section 2 with a review of force measurement in atomic force microscopy, which also serves to establish a consistent nomenclature for subsequent sections. In sections 3 and 4 we review the implementation of the thermal noise and Sader methods, respectively. In section 5 we present our results from measurement of cantilever spring constants over a wide range of conditions and discuss the implications.

2. Measuring forces in AFM

Figure 1(a) provides an overall schematic diagram of an atomic force microscope with optical beam deflection detection (‘optical lever AFM’) while figure 1(b) defines the variables for the cantilever. The normal force of the cantilever on a flat sample, denoted F in figure 1(b), is given by Hooke’s law modified to include the nonzero tilt of the cantilever from [27] (equation (8)):

$$F = \frac{k d_s}{\cos^2 \alpha}, \quad (1)$$

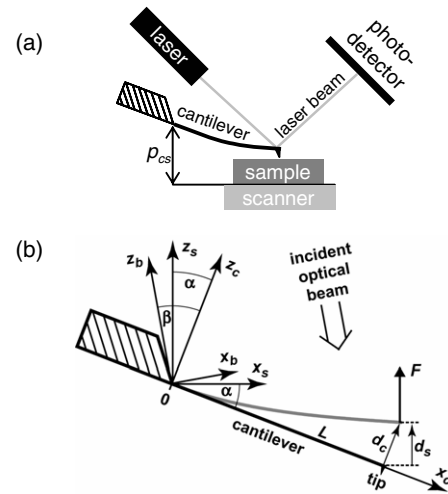


Figure 1. (a) Schematic diagram of an atomic force microscope with optical beam deflection detection (‘optical lever AFM’). (b) Schematic diagram of a deflected cantilever with variable definitions in the scanner (denoted ‘s’), cantilever (denoted ‘c’), and optical beam (denoted ‘b’) reference frames.

where k is the cantilever spring constant, α is the cantilever tilt angle defined in figure 1(b), and d_s is the normal (to the scanner) deflection of the cantilever at its tip with $d_s \equiv 0$ when the cantilever is undeflected. Equation (1) is valid in the limit $\frac{\ell}{L} \rightarrow 0$, where L and ℓ are the lengths of the cantilever and tip respectively. For most cantilevers $\ell \ll L$, which justifies working in this limit. For a discussion of dealing with appreciable tip lengths the reader is referred to [26] and [27].

The tilt angle α in equation (1) is best obtained from design specifications of the instrument. Typical values range from 10° to 15°. Acquisition of d_s is straightforward on most commercial AFMs and is discussed in the remainder of this section.

Measurement of d_s is a standard routine on most commercial AFMs. It is accomplished by taking a ‘force curve’ that measures the change in the photodetector voltage as a function of the separation between the scanner and the base of the cantilever, p_{cs} . Figure 2 shows a typical force curve. In region 1, before the tip is in contact with the surface, the detector voltage is an arbitrary constant independent of p_{cs} , and is determined by the laser beam position on the photodetector. For ease of notation we assume that the voltage has been set to zero in region 1 and denote changes from this zero as V .

In region 2, the tip is in contact with the surface. Provided the surface and tip do not significantly deform, the cantilever deflects at the same rate that it is lowered and $\Delta d_s = \Delta p_{cs}$. Assuming that the scanner has been previously calibrated so that Δp_{cs} is known in metres, measurement of the slope in region 2 provides the conversion factor between detector voltage changes, ΔV , and cantilever deflection in metres, Δd_s . This conversion factor is often referred to as the *sensitivity* or *optical lever sensitivity* defined as

$$\text{sensitivity} \equiv S \equiv \frac{\Delta V}{\Delta d_s}. \quad (2)$$

The sensitivity will change each time the laser beam is repositioned on the cantilever and must be remeasured.

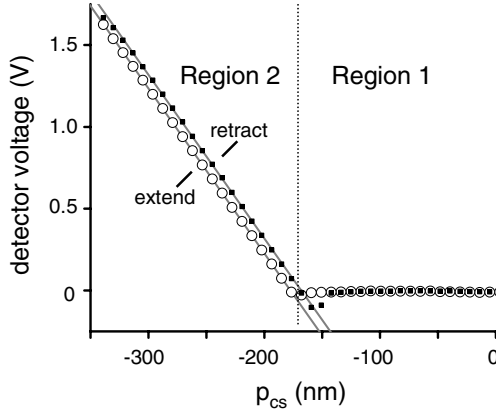


Figure 2. A typical force curve used to determine the sensitivity of the optical lever. The zero of p_{cs} and the detector voltage are set at the initial cantilever–scanner separation. The slope of the lines in region 2 gives the sensitivity, as determined by linear fits to the data shown by the grey lines. For the extension the fit gives a sensitivity $S = 0.01007 \text{ V nm}^{-1}$, while for the retraction $S = 0.00998 \text{ V nm}^{-1}$, a difference of less than 1%. This is a typical percentage difference. To calibrate the optical lever we use the average of the extend and retract sensitivities. The curve was taken on a silicon surface with cantilever E-P1 (see figure 7 and table 1).

Measurement of a given deflection d_s requires knowledge of the detector voltage at that deflection, V , then clearly

$$d_s = \frac{\Delta V}{S} \equiv \frac{V}{S}. \quad (3)$$

Having d_s and α , determination of the normal force exerted by the cantilever requires measurement of the cantilever spring constant, k . The remainder of this paper is devoted to describing two methods for measuring k .

3. Thermal noise method for measuring cantilever spring constants

3.1. Theory and overview

The thermal noise method [20–28] is based on the equipartition theorem from fundamental thermodynamic theory. The equipartition theorem states that for a generalized position or momentum coordinate (denoted here as X) which stores energy according to $E_X \propto X^2$, then the average energy stored in X , $\langle E_X \rangle$, is given by $\frac{1}{2}k_B T$, where k_B is Boltzmann’s constant and T is the absolute temperature [33]. We take ‘ X ’ for the cantilever to be its deflection in its own reference frame, d_c (see figure 1(b)). For small deflections, where the force and deflection are linearly related (as in equation (1)), then the energy stored in this coordinate is given by $\frac{1}{2}k d_c^2$. Thus $\langle E \rangle = \frac{1}{2}k \langle d_c^2 \rangle = \frac{1}{2}k_B T$, and

$$k = \frac{k_B T}{\langle d_c^2 \rangle}. \quad (4)$$

As shown schematically in figure 3, two cantilevers held at the same finite temperature vibrate with amplitudes determined by their respective cantilever spring constants. Thus measuring $\langle d_c^2 \rangle$ and T allows the spring constant to be calculated in

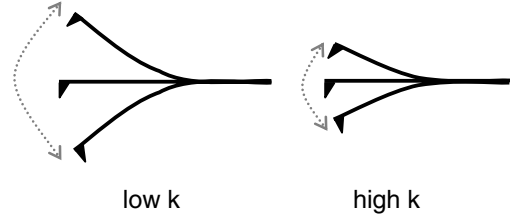


Figure 3. Schematic diagram of thermally driven cantilevers held at the same temperature. According to the equipartition theorem cantilevers with a larger spring constant exhibit a smaller oscillation magnitude. Thus measurement of the average oscillation magnitude yields the cantilever spring constant.

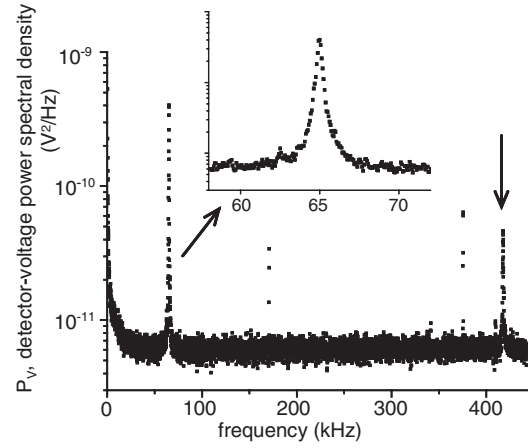


Figure 4. Typical detector-voltage power spectral density. To obtain this curve, 200 time traces of the detector voltage were acquired and Fourier transformed, and the resulting spectra averaged. A zoomed-in view of the lowest cantilever resonance peak is shown in the inset. The second cantilever resonance peak is denoted with a vertical arrow. These data were obtained with cantilever B-P4.

principle. In practice the situation is a bit more complicated, as detailed below.

The remainder of this section simultaneously provides both an overview of and the detailed theory for implementation of the thermal noise method. Subsequent sections detail how to acquire the quantities introduced in this section. Note that the equations presented here are valid only for rectangular cantilevers in the limit $\ell \ll L$, that is tip length not appreciable compared to cantilever length. In addition, the equations require the cantilever to be homogeneous along its length, such that any cross section perpendicular to the length of the cantilever must be identical to any other such cross section. Finally we note that this method is best applied to cantilevers surrounded by vacuum or air, and not to cantilevers in water. Although in principle the method works in water [22], in practice the implementation is more problematic.

The first step in implementing the thermal noise method is to record the thermal vibrations of the cantilever. With the cantilever held far from the sample surface and free to vibrate, the position of the laser beam on the photodetector oscillates. This signal is captured by recording the detector voltage in time, $V(t)$, which can then be Fourier transformed to produce the detector-voltage power spectral density, P_V . An example of P_V is shown in figure 4. In this figure the peaks associated

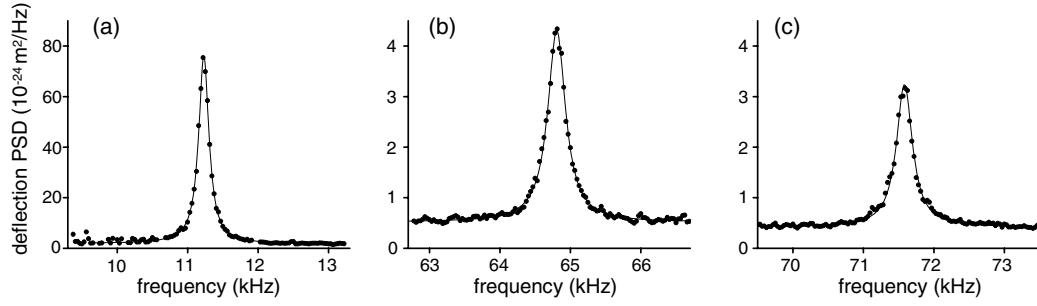


Figure 5. Lowest resonance peaks in the deflection PSD for several cantilevers with different spring constants. The points are data and the solid lines are fits to the data with equation (6). Data in (a) were taken on cantilever G-C1 with $k = 0.19 \text{ N m}^{-1}$, data in (b) were taken on cantilever E-P1 with $k = 2.26 \text{ N m}^{-1}$, and data in (c) were taken on cantilever C-P9 with $k = 3.45 \text{ N m}^{-1}$. Note that the scale in panel (a) is $20\times$ the scale in the other two panels, and the graphs in all three panels span an identical frequency range.

with the two lowest cantilever resonance modes are clearly evident. Implementation of this step is described in detail in section 3.2.

P_V can be converted into the deflection power spectral density (PSD) in the cantilever reference frame, P_d , according to

$$P_d = P_V \frac{1}{S^2} \frac{1}{\cos^2 \alpha} \chi^2. \quad (5)$$

The sensitivity S serves to convert the detector voltage, V , into deflection in the scanner reference frame, d_s . Because $\cos \alpha = \frac{d_s}{d_c}$, the cosine factor subsequently converts to deflection in the cantilever reference frame, d_c .⁴ Measurement of S and α was discussed in section 2.

A full discussion of χ is found in section 3.3. Briefly, the factor χ arises because S was acquired with the cantilever end-loaded, as shown schematically in figure 1(a), while P_V was acquired with the cantilever freely oscillating, as shown schematically in figure 3. The cantilever has slightly different shapes in these two situations, and χ is required to convert the sensitivity from the end-loaded to the freely oscillating shape. In the limit of an infinitely small laser spot positioned precisely on the end of the cantilever, $\chi = 1.09$ [21, 22, 25]; however, not all measurements are made in this limit. For situations not in this limit an online calculator at <http://bioforce.centech.de> gives values of χ . In addition, for the common situation that $\alpha = \beta$ (see figure 1(b)) [25] also provides χ .

Given P_d , it is now possible to find the total power in the thermal vibrations, $\langle d_c^2 \rangle$. If P_d contained no background noise and if the instrument recording it had infinite bandwidth, then $\langle d_c^2 \rangle$ would simply be the integral of P_d over all frequencies, which integral gives the total power in all the resonance peaks. In practice these conditions are never met. Often only the lowest resonance peak is accessible, and background noise may swamp the thermal signal away from that peak. However, the shape of the lowest peak can still provide the required information because it should be well described by the response function for a simple harmonic oscillator

⁴ Note that the factor of $\cos^2 \alpha$ in equation (5) ultimately cancels with the same factor in the force equation (1). Thus it is possible to determine the normal force of the cantilever on the sample without measuring α . This is useful if force, rather than spring constant, is the desired quantity. However, if the factor of $\cos^2 \alpha$ is left out of equation (5), the resulting ‘spring constant’ eventually produced by equation (9) is for a tilted cantilever and cannot be compared with the spring constants determined by the Sader method in section 4.

(SHO) [22]⁵. Thus the lowest resonance peak in P_d should be fitted to the SHO response, R , with an added background term, B :

$$B + R(f) = B + \frac{A_1 f_1^4}{(f^2 - f_1^2)^2 + (\frac{f f_1}{Q_1})^2}, \quad (6)$$

where f_1 and Q_1 give respectively the resonance frequency and quality factor of the lowest peak, and A_1 gives the zero-frequency amplitude of the SHO response. Figure 5 shows the lowest resonance peak for three different cantilevers fitted with equation (6). As demonstrated by the figure, this equation fits the data well.

Integration of the SHO response function, R , over all frequencies gives the ‘spring constant’ when considering only the power in the lowest resonance mode, $\langle d_{c,1}^2 \rangle$. We denote this ‘spring constant’ as k_1 . More explicitly,

$$\int_0^\infty R(f) df = \langle d_{c,1}^2 \rangle = \frac{k_B T}{k_1}. \quad (7)$$

Evaluation of the integral yields $\int_0^\infty R(f) df = \frac{\pi A_1 f_1 Q_1}{2}$, and we thereby obtain

$$k_1 = \frac{2k_B T}{\pi A_1 f_1 Q_1}. \quad (8)$$

Thus k_1 may be obtained from the fit of equation (6) to the lowest resonance peak in P_d .

Because $\langle d_{c,1}^2 \rangle$ does not represent the entire power in the thermal vibrations, k_1 is an overestimate of the real spring constant, k . Using a vibrational mode decomposition of the cantilever oscillations, Butt *et al* [21] found the relationship between the power in the lowest resonance peak and the total power, whence from [21] (equations (21) and (29)), we arrive at an expression for k :⁶

$$k = \frac{k_B T}{\langle d_c^2 \rangle} = \frac{12}{a_1^4} \frac{k_B T}{\langle d_{c,1}^2 \rangle} = 0.9707 k_1 \quad (9)$$

where $a_1 = 1.8751$ per [21] (equation (7)).

⁵ For a classical mechanics text on the simple harmonic oscillator response function see for example [34].

⁶ Some authors [24] have incorrectly used [21] (equation (31)), $k = \frac{4}{3} \frac{k_B T}{\langle d_c^{*2} \rangle}$, to find the spring constant. We note that this equation is valid only when d_c^{*2} is the total power in *all* the resonance peaks in P_d^* . In the nomenclature of Butt, the ‘**’ indicates measurement by the optical lever technique.

In an alternative approach to that described above, in practice we found that a good approximation to $\langle d_{c,1}^2 \rangle$ could often be obtained with a simple numerical integration of the lowest resonance peak in P_d with an appropriate background subtracted. The background may be taken as the mean value of P_d just outside the peak. This approach would not work in all cases. Roughly speaking, if the resonance peak is low and broad or if the noise floor is too high then the numerical integral would not adequately capture all the power in the peak. However, when appropriate, this method may provide a computationally less intensive route to obtaining the spring constant.

As discussed at the beginning of this section, the thermal method described above can only be applied to rectangular cantilevers. However, recent results [35] permit modification of this method for v-shaped cantilevers. Essentially what is required are different values for a_1 and χ , as discussed in [35] and [36]. In addition, we stated that the described thermal method is most accurately applied only to cantilevers in air rather than water. Water damps the oscillating cantilever, thereby lowering its Q_1 , often to order unity [22]. As [43] shows that the SHO function accurately fits the cantilever response only when $Q_1 \gg 1$, use of the thermal method with SHO fit function in water is troublesome. However, [22] does apply this method to the same cantilevers in both air and water and shows an agreement to within $\pm 11\%$.

3.2. Measuring the detector-voltage power spectral density

Having outlined the thermal noise method, we now turn to a more detailed discussion of acquisition of the thermal noise signal. This section describes how to access, record, and Fourier transform the detector-voltage signal $V(t)$. The end result is the detector-voltage power spectral density, P_V , as shown in figure 4.

The first practical challenge is to obtain access to the unfiltered detector-voltage signal. When the cantilever is held far from the sample surface with one end free, its vibrations produce an oscillating voltage from the split-photodetector. In a commercial AFM this signal generally travels from the AFM head to its controller via a multistranded cable. A break-out box allowing interception of the photodetector voltage signal can be purchased from the manufacturer or built. Care must be taken to ensure that any low-pass filters in this line have a corner frequency well above the highest resonance frequency to be measured. Additionally, the electronic path used to capture this signal must have a known gain compared to the path used to record the sensitivity. Finally, to enhance the signal-to-noise ratio in P_V the detector-voltage signal can be passed through a preamplifier. However, as we demonstrate in section 5, external amplification is not always essential to obtain reasonable values for k .

Once the detector-voltage signal has been accessed it needs to be digitized and Fourier transformed. One method to accomplish this is to use a stand-alone commercial spectrum analyser. The disadvantages herein are that a stand-alone spectrum analyser costing about \$5000 is generally limited to frequencies less than 100 kHz, and further, the spectrum analyser must be interfaced with a computer, or the raw data exported, in order to complete the remaining calculations.

However, the advantage to this approach is that the spectrum analyser produces P_V while handling the details of aliasing and windowing discussed below. Further, many cantilevers have fundamental resonance frequencies less than the 100 kHz bandwidth of most analysers.

A second option is to purchase a digitizer card that can be inserted in the AFM control computer. This is the route we chose, using a National Instruments Card NI PCI-5911.⁷ It should be noted that this card is probably faster and more flexible than is typically required. One advantage of this approach is that integrated software, such as National Instruments' Labview (see footnote 7), can control the digitization, Fourier transformation and subsequent analysis to yield the spring constant. A second advantage is that for a few thousand dollars a card can handle a much wider range of frequencies, up to the MHz range, which well exceeds the fundamental resonance frequency of most cantilevers. The disadvantage of this method is that the details of the digitization and Fourier analysis discussed below must be handled in custom-written software. However, pre-written algorithms are available with software packages such as Labview (see footnote 7) and they are fairly easily assembled for these purposes.

One consideration in the choice of digitizer card/spectrum analyser is the range of frequencies that need to be measured. A fairly encompassing range for cantilever resonance frequencies is 10–1000 kHz. The approximate resonance frequency for a particular cantilever can be obtained from the manufacturer. A card to measure a given frequency must be chosen so as to avoid *aliasing*, in which a higher frequency signal appears at a lower frequency due to the digital sampling rate. To avoid aliasing two requirements must be met. First, the *Nyquist criterion* specifies that to measure a maximum frequency f_{\max} , the card/spectrum analyser must have a sample rate, R , such that $R > 2f_{\max}$. Second, to further mitigate aliased signals, *anti-aliasing filters* are required. These are low-pass filters that must have a corner frequency above f_{\max} and below $R/2$. Because no filters can totally eliminate aliasing, to facilitate the filtering in practice it is better if R significantly exceeds $2f_{\max}$. A spectrum analyser will include these filters internally and digitizer cards can be purchased with integrated anti-aliasing filters.

A second consideration in the choice of digitizer card/spectrum analyser is the frequency resolution required. The desired frequency resolution will be determined by the width of the particular peak to be measured. The peaks shown in figure 5 should aid in the choice of required resolution. In general the width of a frequency bin is given by $\Delta f = R/N$, where R is again the sampling rate and N is the number of points in the acquired time domain signal. The choice of card and software must ensure that the signal can be digitized and stored without interruption or loss of data at the chosen rate R . One means to ensure this is to purchase a card with onboard memory that temporarily stores the N data points until the time trace is fully acquired. In this case the on-board memory must be sufficient to store the data required for a given resolution and sampling rate.

⁷ Certain commercial products are identified only to specify the experimental study adequately. This does not imply endorsement by NIST or that the products are the best available for the purpose.

Using either the spectrum analyser or digitizer card the appropriate signal can now be accessed and digitized to yield a single detector-voltage time trace $V(t)$. The time trace can then be Fourier transformed to obtain the appropriate spectrum, $V(f)$, as described in many signal processing texts and standardly available in many commercial software packages. The voltage power spectral density (PSD) is then given by $P_V = \frac{(V_{\text{RMS spectrum}})^2}{\Delta f} = \frac{1}{2} \frac{(V_{\text{Peak spectrum}})^2}{\Delta f}$, where RMS stands for root-mean-square amplitude, Peak stands for peak amplitude, and $\Delta f = R/N$ as discussed above. The units of P_V are $\text{V}^2 \text{Hz}^{-1}$.

One issue that may cause confusion in the acquisition of P_V is the choice and impact of a *windowing function*. Briefly, *windows* are required because the Fourier transform algorithms assume a signal of infinitely long duration as their input. The digitized time-domain signal is clearly not infinitely long; however, one way to make it so is to assume that it repeats an infinite number of times. This potentially creates sharp discontinuities at the interface between the repeating time signals. These sharp discontinuities create spurious signals in the *discrete Fourier transform* (DFT). To avoid artefacts the original time-domain signal may be multiplied by a windowing function that smoothly takes the time signal to a constant value, usually zero, at its first and last point. The sharp discontinuities and spurious signals in the DFT are thus avoided.

The window function itself may introduce some pathologies in the DFT, and so a judicious choice of window should be made for a given signal shape. In practice we tried a number of window functions and found no dependence of the spring constant on the chosen window. An all-around good choice is the Hann (Hanning) window, and this is the window used in our data acquisition.

One of the pathologies introduced by windowing is a spreading of a given frequency component over a range of frequencies, diminishing the component at its proper frequency. To correct for this some spectral analysis systems/software will multiply the spectra by a factor called the *equivalent noise bandwidth* (ENBW) so the spectral peak re-attains its proper value. To determine if this is the case, a single-tone sine wave can be fed into the spectral analysis system. If the resulting spectral peak attains the same value independent of window choice, then the spectrum has been multiplied by the ENBW. If this spectrum is used to compute the power spectral density, the factor must be backed out again to obtain the correct power in the PSD as follows:

$$P_V \text{ (with appropriate power)} = \frac{P_V \text{ (computed from spectrum)}}{\text{ENBW of window}}. \quad (10)$$

The ENBW for the Hann window is 1.5. Fourier analysis software that directly provides the PSD would generally do so without the ENBW factor and therefore with appropriate power.

In this section we have outlined the acquisition of P_V while discussing selected details of the spectral analysis required to obtain it. For more details on digital spectral analysis a wide variety of signal processing texts are available. Among these we found [37] particularly helpful.

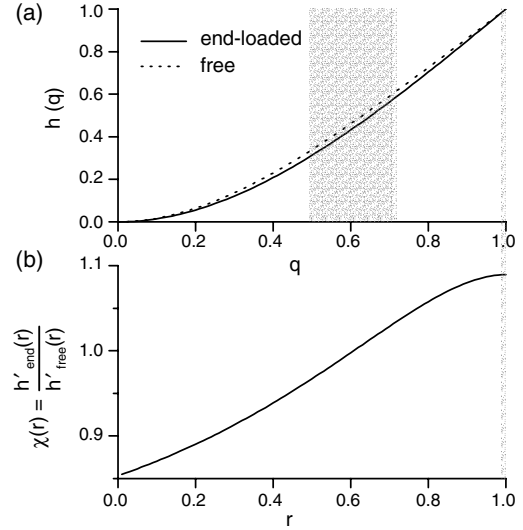


Figure 6. (a) The normalized shape of the lowest mode of both an end-loaded and a freely oscillating cantilever. (b) Ratio of the slopes of the end-loaded to the freely oscillating cantilever, showing the variation of χ as a function of laser beam position, r , for an infinitely small optical spot size. For a finite spot size, such as that depicted schematically by the grey shaded area centred at $q = 0.6$, the value of χ is determined by the finite size of the optical spot and by the shape of the cantilever in the region illuminated by the spot. For a split photodetector the appropriate equations are outlined in section 3.3 and given in [25] and [38].

3.3. Origin and value of χ

This section discusses the factor χ which appears in equation (5). We explain its origin and then discuss means to determine the appropriate value for a given measurement. The discussions in this section are valid only for the lowest resonance peak of a rectangular cantilever.

The shape of the cantilever differs when it is freely oscillating as compared to end-loaded, and the correction factor, χ , is required to convert between these situations. Following the derivation of [25] and [38], we consider the shape of the cantilever in each situation. The end-loaded shape of the lowest mode is given by [39]

$$h_{\text{end}}(q) = \frac{3q^2 - q^3}{2}, \quad (11)$$

where h_{end} gives the normalized deflection of the cantilever in its own reference frame, and h_{end} and q are normalized such that at the cantilever base $q = 0$ and $h_{\text{end}}(0) = 0$ and at the cantilever end $q = 1$ and $h_{\text{end}}(1) = 1$. Similarly, the normalized shape of the freely oscillating cantilever is given by

$$h_{\text{free}}(q) = 0.5000(\cosh a_1 q - \cos a_1 q) - 0.3670(\sinh a_1 q - \sin a_1 q), \quad (12)$$

where $a_1 = 1.8751$. These two shapes are shown in figure 6(a).

The detection sensitivity S , defined in equation (2), is obtained with an end-loaded cantilever, as shown schematically in figure 1(a). We thus more accurately write $S \equiv S_{\text{end}}$. In contrast, the detector-voltage power spectral density P_V was acquired with the cantilever freely vibrating, as shown schematically in figure 3. To appropriately convert

P_V to P_d , we require a sensitivity obtained with a freely vibrating cantilever, denoted as S_{free} . However, S_{free} is not an experimentally obtainable quantity. This situation is resolved by taking the ratio of the theoretically obtained end-loaded and freely oscillating sensitivities denoted as σ_{end} and σ_{free} to obtain a scaling factor:

$$\chi \equiv \frac{\sigma_{\text{end}}}{\sigma_{\text{free}}}. \quad (13)$$

This theoretically obtained factor is then used to scale the experimentally obtained values according to $S_{\text{free}} \equiv \frac{S_{\text{end}}}{\chi}$.

To obtain an appropriate value for χ , both the size and placement of the optical spot on the cantilever must be considered. Until recently most researchers have used a value of $\chi = 1.09$, which is strictly valid only in the limit of an infinitely small optical spot precisely positioned on the end of the cantilever. Use of this value may introduce an error of a few per cent for longer cantilevers ($L > \approx 200 \mu\text{m}$), while for shorter cantilevers the introduced error is much larger. For explanatory purposes we begin by explaining the origin of χ in this limit of an infinitely small optical spot. We subsequently discuss appropriate means to obtain χ when not in this limit.

The value for χ in the small optical-spot limit is obtained by considering the origin of the photodetector output. In the optical lever set-up for an AFM (see figure 1(a)), the cantilever's slope at the reflection point of the laser beam, r , determines the laser beam position on the photodetector [39]. (Note that r is given in the cantilever reference frame and is normalized to the total cantilever length.) Accordingly, the photodetector output, and hence the sensitivity, for a given cantilever shape is determined by the cantilever slope for that shape evaluated at r , given as $h'(r) = \frac{dh(q)}{dq}|_{q=r}$, and thus

$$\chi(r) \equiv \frac{\sigma_{\text{end}}(r)}{\sigma_{\text{free}}(r)} = \frac{h'_{\text{end}}(r)}{h'_{\text{free}}(r)}. \quad (14)$$

This ratio is plotted in figure 6(b). When the infinitely small optical spot reflects at $r = 1$ it samples only the slope at the end of the cantilever, and then

$$\chi = \chi(1) = \frac{\sigma_{\text{end}}(1)}{\sigma_{\text{free}}(1)} = \frac{h'_{\text{end}}(1)}{h'_{\text{free}}(1)} = 1.09. \quad (15)$$

This is shown schematically in figure 6(b) as the narrow grey shaded area at $r = 1$.

The value for χ in this limit was originally indirectly suggested by Butt and Jaschke [21] using a vibrational mode analysis. Walters *et al* [22] pointed out that this factor could be obtained by using the ratio of [21] (equation (21)) to (equation (25)) to obtain

$$\chi_i(1) = \sqrt{\frac{\langle z_i^2 \rangle}{\langle z_i^{*2} \rangle}} = \frac{3}{2a_i} \left(\frac{\sin a_i + \sinh a_i}{\sin a_i \sinh a_i} \right), \quad (16)$$

where the index i gives the resonance peak number, and a_i is a constant determined by the boundary conditions of the cantilever. For the lowest resonance peak of a rectangular cantilever free at one end [21] (equation (7)) finds $a_1 = 1.8751$ and hence $\chi_1(1) = 1.09$. To more intuitively understand the above derivation, consider that the ratio of [21] (equation (19)) to (equation (22)) is also equivalent to equation (16) above.

When the laser optical spot is not at the end of the cantilever or is not in the limit of infinitely small, the value of χ is not 1.09. This situation is shown schematically in figure 6(b) by an optical spot that covers the grey shaded area centred at $r = 0.6$. (We now take r to denote the centre of the optical spot in the cantilever reference frame.) In this case the optical spot samples slopes along the illuminated region of the beam. In a 'continuous' photodetector, such as one that can be constructed using an array photodetector [40, 41], the values of the theoretical sensitivities, σ_{end} and σ_{free} , turn out, as one might intuitively suspect, to be the weighted average of the respective slope over the grey shaded region. The weighting function is given by the laser beam irradiance profile, usually taken as Gaussian. See [41] (equations (14) and (15)) for further details. In the case of the commonly used split-photodetector, the idea is similar but the split produces different equations for the theoretical sensitivities. The end result for the theoretical sensitivity is given in [38, 41], and [42]. Using these results, χ can be expressed for a split-photodetector as

$$\chi(\Delta, r) \equiv \frac{\sigma_{\text{end}}(\Delta, r)}{\sigma_{\text{free}}(\Delta, r)} = \frac{f_{\text{end}}(\Delta, r)}{f_{\text{free}}(\Delta, r)} \quad (17)$$

$$f_x(\Delta, r) = \frac{4}{\pi \Delta^2} \int_0^1 dq \int_0^1 dq' \frac{h_x(q) - h_x(q')}{q - q'} \times \exp \left[\frac{-4(q-r)^2 - 4(q'-r)^2}{\Delta^2} \right], \quad (18)$$

where x denotes *end* or *free*, $\Delta = \frac{w}{L \cos \beta}$, and w is the $\frac{1}{e^2}$ diameter of the optical spot irradiance profile in the beam reference frame. An online calculator at <http://bioforce.centech.de> allows the calculation of χ and several other factors. For the common situation in which $\alpha = \beta$, [25] (figure 5) gives values for χ as a function of optical spot size and position. We note that our variable r corresponds to ' x_c/L_{eff} ' in the nomenclature of [25] (when $\alpha = \beta$) and corresponds to ' p_b/L_{eff} ' in the nomenclature of [38] (for arbitrary α and β).

4. Sader method for measuring cantilever spring constants

The Sader method is based on the theory of a driven cantilever's response in a fluid of known density and viscosity [31, 43]. Typically the fluid is air. From modelling the effect of fluid dissipation on the cantilever response, the spring constant is given by [30]

$$k = 7.524 \rho_f b^2 L Q_1 f_1^2 \Gamma_i(\rho_f, \eta_f, f_o, b), \quad (19)$$

where ρ_f and η_f are respectively the density and viscosity of the fluid, b and L are respectively the width and length of the cantilever, Q_1 and f_1 are respectively the quality factor and frequency of the lowest resonance peak as measured in the fluid, and Γ_i is the imaginary component of a hydrodynamic function given by [43] (equation (20)). The website <http://www.ampc.ms.unimelb.edu.au/afm> provides an online calculator and downloadable Mathematica (see footnote 7) notebooks for equation (19).

Equation (19) is valid for rectangular cantilevers in the limit that the length of the cantilever L greatly exceeds its width b , which in turn greatly exceeds its thickness. These requirements are generally met for common rectangular

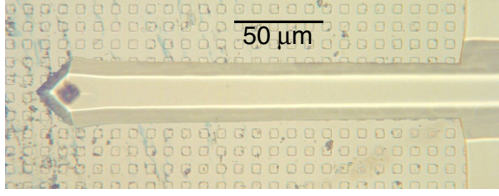


Figure 7. Photograph of cantilever E-P1 overlaid on photograph of 10 μm pitch calibration grid used in measuring the cantilever length and width. Both photographs were taken with the same optical microscope under the same magnification.

(This figure is in colour only in the electronic version)

cantilevers. Validity of equation (19) further requires that the quality factor Q_1 greatly exceed unity. This requirement is generally met for cantilevers measured in air. Finally, equation (19) requires that the cantilever be homogeneous along its length.

Methods of acquiring the required quantities, ρ_f , η_f , b , L , Q_1 and f_1 are relatively straightforward. The resonance frequency, f_1 , and quality factor, Q_1 , for the cantilever are obtained from the fit of P_d to equation (6), as discussed in section 3.1. The width b and length L of the cantilevers may be easily measured with an optical microscope. A picture of a cantilever and of a calibration grid are obtained with the same magnification. As shown in figure 7, the pictures are then overlaid. In practice, to find L we measure the length of the cantilever from the tip (including the tapered region) to the base (where the cantilever contacts the substrate). To find b , we measure the widest part of the cantilever (not in the tapered region). As discussed in section 5, this manner of measuring may produce a slight overestimate of the appropriate effective length and width.

If the spring constant is measured with air as the known fluid, the variation ρ_f and η_f with ambient temperature and pressure should be considered. The most significant variation is that of air density with the air pressure at the local elevation. To find the local air density ρ_{air} , measure the total air pressure, P , and temperature, T , near the AFM and use the ideal gas law to find

$$\rho_{\text{air}}(P, T) = \frac{PM}{RT}, \quad (20)$$

where the typical molar mass of air is $M = 0.02897 \text{ kg mol}^{-1}$ and the molar gas constant $R = 8.31441 \text{ J mol}^{-1} \text{ K}^{-1}$. In our facility in Boulder, CO, (elevation 1650 m) we measured the total air pressure P and temperature T near the AFM to be $8.46 \times 10^4 \text{ Pa}$ and 293.4 K respectively, and thus we use $\rho_{\text{air}} = 1.00(5) \text{ kg m}^{-3}$. For a standard sea-level atmospheric pressure of $1 \text{ atm} = 10.133 \times 10^4 \text{ Pa}$ and ambient temperature of $20.0^\circ\text{C} = 293.15 \text{ K}$, then $\rho_{\text{air}} = 1.204 \text{ kg m}^{-3}$. The viscosity of air η_f is independent of air pressure for all ambient pressures, and at 20.0°C , $\eta_f = 1.84 \times 10^{-5} \text{ kg m}^{-1} \text{ s}^{-1}$.

As discussed at the beginning of this section, the Sader method described above can only be applied to rectangular cantilevers. However, [30] and [31] do describe two methodologies, both requiring additional measurements, which permit the application of this method to v-shaped cantilevers. In addition, we stated that the described Sader method is valid only when $Q_1 \gg 1$, or essentially when measurements are

made in air rather than water. This restriction arises for the same reason as in the thermal method. Water damps the cantilever oscillations potentially to order unity [22], and the SHO fit, which determines Q_1 and f_1 , is only accurate in the high Q_1 limit [43].

5. Results

To compare the thermal noise and Sader methods, we measured a variety of cantilevers by both methods. Table 1 provides a comprehensive list of cantilevers measured. To obtain the data in the table, each cantilever was photographed under a microscope (e.g. figure 7) to obtain its length and width. It was then mounted in our Veeco Metrology/Digital Instruments Dimension 3000 AFM (see footnote 7), and a force curve (e.g. figure 2) was taken on a standard sample. The sensitivity was determined by fitting both the extend and retract curves in the contact region (Region 2 in figure 2) and averaging these two slopes.

The cantilever was then held far from the sample and the oscillating voltage from the photodetector was passed directly to a DAQ card in our AFM control computer. We chose not to use an intermediate preamplifier in order to demonstrate that a minimally complicated set-up is sufficient to produce reasonable values for the spring constant of many standard cantilevers⁸. To obtain a spectrum like that shown in figure 4 we acquired and Fourier transformed 200 time traces (as described in section 3.2) and then averaged the resulting 200 spectra to obtain P_V . We acquired six P_V curves for each cantilever.

Each P_V curve was transformed to P_d according to equation (5). To this end, we obtained from our AFM manufacturer a value of $\alpha = 13^\circ$ for the cantilever tilt angle and a profile of $30 \mu\text{m} \times 15 \mu\text{m}$ (long axis of the ellipse along the length of the cantilever) for the optical spot size. Although unconfirmed by the manufacturer, we assumed that $\alpha = \beta$. Using the measured cantilever lengths (L), we were then able to calculate the appropriate value of χ from equations (17) and (18).

Having now obtained P_d , we fitted its lowest resonance peak with equation (6) as shown in figure 5, and the thermal noise spring constant was acquired according to equations (7)–(9). Using Q_1 and f_1 from the fit and L and b from the microscope photograph, the Sader method spring constant was determined by equation (19). The average of the six measured spring constants for each method and cantilever is shown in table 1. All measurements were made in air at room temperature.

In figure 8 we plot the average cantilever spring constant obtained by the thermal noise method versus that obtained by the Sader method from the data of table 1. The grey line represents equality between the two methods, and the data lie substantially along this line, thus demonstrating consistency between the methods. To quantify the consistency we define the percentage difference between methods as

$$\delta \equiv 100 \frac{\text{Thermal } k - \text{Sader } k}{\frac{1}{2}(\text{Thermal } k + \text{Sader } k)}. \quad (21)$$

⁸ To view spectra with a higher signal-to-noise ratio than that of figure 4 the reader is referred to [22] (figure 2).

Table 1. Description and results for measured cantilevers. Cantilevers are designated by a code such as E-P1 which specifies the first cantilever from wafer E of type P, where the type is specified by manufacturer, part number, material and coating in subsequent columns. The legend in the far left column is keyed to figure 8(a). The length (L), width (b), lowest resonance frequency and quality factor (f_1 and Q_1) are measured as detailed in the text. The ‘Nom. k ’ values are those given by the manufacturer for the type, while the Sader and thermal noise k values are measured as discussed in the text.

Symbol	Cantilever	Manufacturer	Part number	Material	Front side coating	Back side coating	L (μm)	b (μm)	f_1 (kHz)	Q_1	Nom. k (N m^{-1})	Sader k (N m^{-1})	Thermal noise k (N m^{-1})	δ (%)
★	A-ESP4 A-ESP5	Veeco	ESP	Si	None	50 nm Al	470 473	41 41	14.0 12.0	57.9 49.5	0.2	0.17 0.12	0.17 0.10	−2.9 −17.6
◆	G-C1 G-C2	Veeco	SCM-PIC	Si	3 nm Cr + 20 nm PtIr5	3 nm Cr + 20 nm PtIr5	490 495	62 61	11.2 11.5	61.5 65.9	0.2	0.19 0.21	0.19 0.21	−4.4 −3.3
▽	A-M1 A-M2	Veeco	MPP-32100	Si	None	None	448 448	33 33	17.1 17.4	68.9 69.3	0.1	0.22 0.23	0.20 0.20	−9.0 −11.1
△	A-F1a	Veeco	CLFC	Si	None	None	401	25	16.6	52.3	0.16	0.12	0.12	0.7
▲	A-F1b						200	25	65.1	125.2	1.3	0.90	0.96	6.9
▲	A-F1c						103	23	245.7	290.9	10.4	6.72	6.82	1.5
□	A-A1 A-A2	Olympus	AC240 TM-B2	Si	Pt	Al	238 235	28 28	53.7 54.1	140.3 138.4	2	1.02 1.00	1.04 1.04	3.0 3.9
⊖	A-P4	Veeco	SCM-PIT	Si	3 nm Cr + 20 nm PtIr5	3 nm Cr + 20 nm PtIr5	247	32	47.5	149.7		1.04	0.84	−21.3
⊕	B-P4						244	33	65.0	196.8		2.17	2.47	13.0
○	C-P8						243	38	72.7	258.6		3.74	3.30	−12.4
○	C-P9						245	38	71.6	255.5		3.68	3.45	−6.2
○	C-P7						243	36	76.8	274.3	2.8	4.14	4.32	4.6
●	D-P3						240	30	58.7	170.9		1.50	1.40	−6.8
⊕	E-P1						245	34	64.8	218.4		2.48	2.26	−9.2
⊕	E-P2						242	37	66.0	209.0		2.59	2.35	−9.7
●	F-P1						240	33	52.1	173.4		1.39	1.41	1.9
●	F-P2						244	34	53.5	168.9		1.44	1.31	−8.8

For the cantilevers described in table 1 the mean value and standard deviation of δ are $-4.2\% \pm 8.4\%$, demonstrating a consistency between the methods to well within the previously quoted accuracy of $\sim 10\%$ – 20% for each individual method [22, 25, 30, 32]. Thus we conclude that the two methods agree well over almost two orders of magnitude on this disparate set of cantilevers. Because the two methods are derived from distinct physics, the agreement is a compelling argument in favour of the accuracy and utility of both methods.

Although the agreement between the two methods is good, we observe a trend toward higher k values obtained by the Sader as compared to the thermal noise method. This is manifest in the negative mean value of δ and equivalently in the data points lying more than one standard deviation below the equality line, as seen clearly in figures 8(b) and (c). This trend suggests a systematic error, for which we postulate two potential origins.

First, the systematic error may derive from the shape of our cantilevers. While the Sader method is strictly valid only for rectangular cantilevers, the majority of our cantilevers have a short tapered region near their end, as seen in figure 7. The extent of this tapered region is typically between $0.05L$ and $0.1L$. Although we are not aware of an explicit theory, it seems reasonable to assume an effective length of $0.9L$ – $1L$ for a cantilever with an $0.1L$ tapered region. As equation (19) is linear in L , this up to 10% reduction in effective length for a given cantilever would reduce the value of k derived from the Sader method, and thus increase the value of δ , by a similar amount. To further substantiate this argument, we measured three cantilevers without tapered regions, A-F1a, A-F1b, and A-F1c. The values of δ for these three cantilevers

were respectively 0.7%, 6.9% and 1.5%, substantially differing from the negative average value of δ . Although this observation is by no means conclusive, taken together with the argument above, it does suggest that consideration of the tapered regions would be sufficient to account for the observed systematic difference between methods.

Second, the systematic error may derive from the calibration of our scanner, since the thermal noise method is dependent upon the scanner calibration to accurately measure $\Delta p_{cs} = \Delta d_s$. Shortly before making the spring constant measurements presented here we calibrated our scanner using a standard calibration grid (shown in figure 7) and routines provided by the AFM manufacturer. A quantitative discussion of the uncertainties involved in this process is beyond the scope of this paper, and the reader is referred to [44]. However, any uncertainty in the calibration would manifest itself as a systematic error, and thus this may account for some of the observed systematic difference between the two methods.

We focus now on panels 8(b) and (c) to discuss the scatter in each method. Determination of the sensitivity could potentially introduce a statistical error. To estimate the magnitude of this error, we mounted a single cantilever, similar in dimension to that pictured in figure 7, and a relatively inexperienced operator was asked to repeatedly reposition the laser on the end of the cantilever. A force curve was obtained after each reposition and, as in figure 2, the slopes of the *extend* and *retract* curves in Region 2 were obtained and averaged. Nine such trials produced an average sensitivity S and respective standard deviation ΔS such that $100(\frac{\Delta S}{S}) \approx 2\%$. We take this value as representative of the statistical error introduced by the sensitivity measurement.

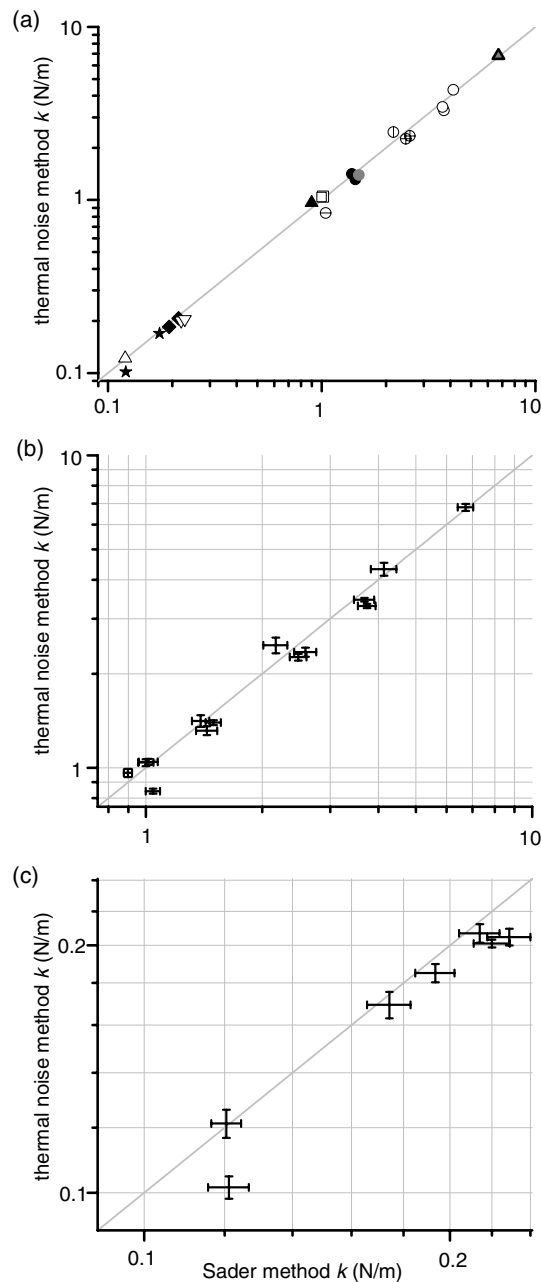


Figure 8. Measured value of the spring constant by thermal versus Sader method. The 45° grey line in all panels represents equality between the methods. In (a) we plot data from all the cantilevers detailed in table 1 with the legend for this plot given in the table. The data lie nicely along the equality line, demonstrating agreement between the two methods over almost two order of magnitude in k . In addition, like symbols represent cantilevers from the same wafer, while like shapes represent cantilevers of the same type (manufacturer part number), thus variation in k between ostensibly similar cantilevers can be easily observed in this panel. In (b) and (c) we zoom in respectively on the higher and lower k regions of (a). The error bars in these panels represent the standard deviation obtained from six measurements of each cantilever. As discussed in the text, they represent the size of the dominant statistical error.

We also consider variation in the P_d spectra themselves. This variation can be somewhat reduced by a significantly longer averaging time in the acquisition of P_V or by acquiring

a much higher resolution spectrum. However, in keeping with the practical focus of this paper, we did not find the tradeoff in acquisition time worthwhile for the small improvement in scatter. For both methods we measure variation in P_d by variation in the final values of k obtained from the multiple acquired spectra. For each method the average scatter was measured by taking the standard deviation Δk from the six P_d curves acquired for each cantilever and then averaging over all the cantilevers to find for the thermal method $100\langle\frac{\Delta k}{k}\rangle \approx 3\%$, while for the Sader method the same exercise produced $100\langle\frac{\Delta k}{k}\rangle \approx 5\%$. In the case of the Sader method this scatter was entirely determined by the scatter in Q_1 from the fits. In both cases this scatter is representative of the overall statistical error in the measurement since it dominates over that introduced by the sensitivity measurements. Thus the statistical error represented by the error bars in figures 8(b) and (c) is derived from Δk .

In addition to showing consistency between the two methods, figure 8 also presents a persuasive case for the need to measure cantilever spring constants rather than relying upon manufacturer specifications. In figure 8(a) like shapes (e.g. circles) represent cantilevers of the same type (manufacturer part number) while like symbols (e.g. filled circles) represent cantilevers of the same type that were also co-fabricated on the same wafer. Consider the cantilever type represented by circles, which has a manufacturer specified spring constant of 2.8 N m^{-1} with a specified maximum range of $1\text{--}5 \text{ N m}^{-1}$. As seen in the figure, a random sampling of cantilevers from six different wafers produced spring constants nearly spanning this range. Even considering cantilevers co-fabricated on the same wafer, the variation is significant. The open circles (C-P series) and the stars (A-ESP series) represent two examples of significant variation in k ($\sim 50\%$ difference between the A-ESP cantilevers) for nominally identical co-fabricated cantilevers.

In summary, knowledge and control of the forces exerted by an AFM cantilever are essential for many applications, and measurement of individual AFM cantilever spring constants is essential for this purpose. In this paper we thoroughly detail the implementation of two particularly advantageous methods for measuring spring constants, the thermal noise and Sader methods. Upon using the two techniques to measure a variety of cantilevers over almost two orders of magnitude of k , we find good agreement between them. As the methods are derived from distinct physics, we feel this is a compelling argument in favour of the accuracy of both. Given the ability of both techniques to give an *in situ*, non-destructive, fast measurement of k for a cantilever independent of its material or coating, we recommend these methods, where applicable, as the practical standards for the field.

Acknowledgments

We thank Sae Woo Nam and Tracy Clement for their insightful comments. We especially thank David Pappas for his many contributions. The authors express their appreciation to the following agencies for their financial support: ARDA under Contract No. MOD717304 (NIST contributors), Gemeinnützige Hertie-Stiftung/Stifterverband für die Deutsche Wissenschaft (TES), Colorado College

Faculty Research Funds (Colorado College contributors) and Petroleum Research Fund Grant number 41739-GB5 (KML).

Contribution of the US government. Not subject to copyright.

References

- [1] Lang K M, Hite D A, Simmonds R W, McDermott R, Pappas D P and Martinis J M 2004 *Rev. Sci. Instrum.* **75** 2726
- [2] Lantz M A, O'Shea S J and Welland M E 1997 *Phys. Rev. B* **56** 15345
- [3] Florin E-L, Moy V T and Gaub H E 1994 *Science* **264** 415
- [4] Moy V T, Florin E L and Gaub H E 1994 *Science* **266** 257
- [5] Lee G U, Kidwell D A and Colton R J 1994 *Langmuir* **10** 354
- [6] Dammer U, Popescu O, Wagner P, Anselmetti D, Guntherodt H and Misevic G N 1995 *Science* **267** 1173
- [7] Hinterdorfer P, Baumgartner W, Gruber H J, Schilcher K and Schindler H 1996 *Proc. Natl Acad. Sci. USA* **93** 3477
- [8] Grandbois M, Beyer M, Rief M, Clausen-Schaumann H and Gaub H E 1999 *Science* **283** 1727
- [9] Lee G U, Chrisey L A and Colton R J 1994 *Science* **266** 771
- [10] Rief M, Gautel M, Oesterhelt F, Fernandez J M and Gaub H E 1997 *Science* **276** 1109
- [11] Rief M, Oesterhelt F, Heymann B and Gaub H E 1997 *Science* **275** 1295
- [12] Clifford C A and Seah M P 2005 *Nanotechnology* **16** 1666
- [13] Gibson C T, Watson G S and Myhra S 1996 *Nanotechnology* **7** 259
- [14] Jericho S K and Jericho M H 2002 *Rev. Sci. Instrum.* **73** 2483
- [15] Cumpson P J, Hedley J and Zhdan P 2003 *Nanotechnology* **14** 918
- [16] Li Y Q, Tao N J, Pan J, Garcia A A and Lindsay S M 1993 *Langmuir* **9** 637
- [17] Rabinovich Ya I and Yoon R-H 1994 *Langmuir* **10** 1903
- [18] Senden T J and Ducker W A 1994 *Langmuir* **10** 1003
- [19] Cleveland J P, Manne S, Bocek D and Hansma P K 1993 *Rev. Sci. Instrum.* **64** 403
- [20] Hutter J L and Bechhoefer J 1993 *Rev. Sci. Instrum.* **64** 1868
- [21] Butt H-J and Jaschke M 1995 *Nanotechnology* **6** 1
- [22] Walters D A, Cleveland J P, Thomson N H, Hansma P K, Wendman M A, Gurley G and Elings V 1996 *Rev. Sci. Instrum.* **67** 3583
- [23] Lévy R and Maaloum M 2002 *Nanotechnology* **13** 33
- [24] Burnham N A, Chen X, Hodges C S, Matei G A, Thoreson E J, Roberts C J, Davies M C and Tendler S J B 2003 *Nanotechnology* **14** 1
- [25] Proksch R, Schäffer T E, Cleveland J P, Callahan R C and Viani M B 2004 *Nanotechnology* **15** 1344
- [26] Heim L-O, Kappl M and Butt H-J 2004 *Langmuir* **20** 2760
- [27] Hutter J L 2005 *Langmuir* **21** 2630
- [28] Schäffer T E 2005 *Nanotechnology* **16** 664
- [29] Sader J E, Larson I, Mulvaney P and White L R 1995 *Rev. Sci. Instrum.* **66** 3789
- [30] Sader J E, Chon J W M and Mulvaney P 1999 *Rev. Sci. Instrum.* **70** 3967
- [31] Sader J E, Pacifico J, Green C P and Mulvaney P 2005 *J. Appl. Phys.* **97** 124903
- [32] Sader J E 2002 *Encyclopedia of Surface and Colloid Science* (New York: Dekker) p 846
- [33] See for example: Schroeder D V 2000 *Thermal Physics* (New York: Addison-Wesley)
- [34] Marion J B and Thornton S T 1995 *Classical Dynamics of Particles and Systems* 4th edn (Orlando, FL, USA: Harcourt Publishers) chapter 3
- [35] Stark R W, Drobek T and Heckl W M 2001 *Ultramicroscopy* **86** 207
- [36] Butt H-J, Cappella B and Kappl M 2005 *Surf. Sci. Rep.* **59** 1
- [37] Harvey A F and Cerna M, The fundamentals of FFT-based signal analysis and measurement in LabVIEW and LabWindows/CVI *National Instruments Application Note* 041 (www.nationalinstruments.com)
- [38] Schäffer T E and Fuchs H 2005 *J. Appl. Phys.* **97** 083524
- [39] Sarid D 1994 *Scanning Force Microscopy: With Applications to Electric, Magnetic and Atomic Forces* 2nd edn (New York: Oxford University Press)
- [40] Schäffer T E, Richter M and Viani M B 2000 *Appl. Phys. Lett.* **76** 3644
- [41] Schäffer T E 2002 *J. Appl. Phys.* **91** 4739
- [42] Schaffer T E and Hansma P K 1998 *J. Appl. Phys.* **84** 4661
- [43] Sader J E 1998 *J. Appl. Phys.* **84** 64
- [44] Gibson C T, Watson G S and Myhra S 1997 *Scanning* **19** 564